Poincaré-beam patterns produced by nonseparable superpositions of Laguerre–Gauss and polarization modes of light

Enrique J. Galvez,* Shreeya Khadka, William H. Schubert, and Sean Nomoto

Department of Physics and Astronomy, Colgate University, Hamilton, New York 13346, USA

*Corresponding author: egalvez@colgate.edu

Received 3 January 2012; revised 20 February 2012; accepted 24 February 2012;
posted 24 February 2012 (Doc. ID 160783); published 16 May 2012

We present a study of Poincaré-beam polarization patterns produced by collinear superposition of two Laguerre–Gauss spatial modes in orthogonal polarization eigenstates (circular or linear). We explore theoretically and experimentally the combinations that are possible. We find that the resulting patterns can be explained in terms of mappings of points on the Poincaré sphere onto points in the transverse plane of the beam mode. The modes that we produced yielded many types of polarization singularities. © 2012 Optical Society of America

OCIS codes: 260.5430, 260.6042.

1. Introduction

Poincaré beams have a spatial mode that correlates transverse spatial coordinates with states of polarization. The state of polarization may vary along one coordinate. For example, in radial vector beams, the state of linear polarization varies along the angular coordinate so that the polarization direction at any point is parallel to the radial direction [1–6]. The state of polarization may depend on the two transverse coordinates. This case, first referred to as full Poincaré beams [7], in which the state of polarization varies both in the angular and radial coordinates, leads to a transverse mode that has all states of polarization, as represented on the Poincaré sphere.

In general, Poincaré and vector modes are nonseparable superpositions of spatial and polarization modes. Past work on vector beams involved using either the superposition of first-order Hermite–Gauss modes with orthogonal linear polarization or Laguerre–Gauss modes of the same order with orthogonal circular polarization [3,8,9]. Both types of construction involved the use of interferometers to combine the two beams. Other approaches to generate vector beams involve intra-laser-cavity elements [1,4], external electro-optical or diffractive optical elements [2,10,11], nonlinear elements [12], optical fibers [13–15], or optical elements with stress birefringence [7].

The applications of vector beams have been limited to the simplest types of modes, radial or azimuthal (linear polarization is perpendicular to the radial directions), for use in either charged-particle acceleration [16] or manipulation with optical tweezers [17]. The exploration of a greater variety of polarization patterns offered by Poincaré modes, as presented in this article, promises more applications in optical manipulation and topological diagnosis of inhomogeneous media.

Poincaré beams are of intrinsic interest because they carry polarization singularities. These are points in space that are elliptic dislocations of a vector field, in this case, the electromagnetic field [18–21]. There have been a number of recent studies on producing and measuring polarization singularities via passage of light through inhomogeneous birefringent media [22–28]. Recent reports tailor the

1559-128X/12/152925-10$15.00/0

polarization-singularity analysis via production of Poincaré beams [7,12]. With Poincaré beams we can study these topological features by producing them deliberately in the laboratory [29].

In this article we study Poincaré beams by exploring all possible combinations of high-order Laguerre–Gauss modes that can be used to make up distinct spatial-polarization modes and different types of polarization singularities. We show methods to produce Poincaré modes with single or multiple mappings of the Poincaré sphere onto the transverse plane of a light beam. Our experimental work focuses on combining two pure Laguerre–Gauss beams collinearly with an interferometer. Analytically, we explore all cases, including high-order radial modes. In Section 2 we present a theoretical framework for the description of Poincaré modes with Laguerre–Gauss spatial modes. Section 3 describes our experimental method. Our analysis of the Poincaré modes with our measurements is presented in Section 4. These are subdivided in a way to highlight important types of spatial-polarization patterns. Section 5 has discussion and conclusions.

2. Theoretical Formalism

In this section we present a few definitions.

A. Spatial Modes

A Laguerre–Gauss mode with radial subindex p and azimuthal index ℓ is given, in cylindrical coordinates (r,ϕ,z), by [30]

$$LG_p^\ell = A_{p,\ell} r^{|\ell|} e^{i\ell\phi} G L_p^{|\ell|} W_{p,\ell}, \tag{1}$$

where

$$A_{p,\ell} = \left(\frac{p!2^{|\ell|+1}}{\pi(|\ell|+p)!}\right)^{1/2} \frac{1}{w^{|\ell|+1}} \tag{2}$$

is a normalization constant;

$$G = e^{-r^2/w^2} \tag{3}$$

is the Gaussian envelope, with w being the beam width (or spot); $L_p^{|\ell|}$ is the associated Laguerre function of $2r^2/w^2$; and

$$U_{p,\ell} = e^{i(x^2+y^2)/(2R)-i\varphi} \tag{4}$$

is a term containing overall phase information, with R being the radius of curvature of the wavefront and

$$\varphi = (2p+|\ell|+1)\tan^{-1}(z/z_R) \tag{5}$$

being the Gouy phase with z_R the Rayleigh range. The order of the mode is $N = 2p+|\ell|$. For practical reasons we will consider the width of the beam $w = 1$, and the phase term $U_{p,\ell} = 1$ for the remainder of this article. In Section 5 we discuss the effect of $U_{p,\ell} \neq 1$.

The modes with $p = 0$ are, with exception of $\ell = 0$, singly ringed with a peak at

$$r_\ell = \left(\frac{\ell}{2}\right)^{1/2}. \tag{6}$$

Modes with $p \neq 0$ are multiringed. For example, $p = 1$, $\ell = 0$ modes have a maximum at $r = 0$, a zero crossing at $r = 1/\sqrt{2}$, and another maximum at $r = \sqrt{3/2}$; whereas $p = 1$, $\ell \neq 0$ have a minimum at $r = 0$ and two extrema (e.g., $r = 0.47$ and $r = 1.51$ for $\ell = 1$) separated by a zero crossing at $r = \sqrt{(|\ell|+1)/2}$.

B. Polarization States

For states of polarization, we are going to use an uncommon notation, so we present it here. The states of polarization are represented by points on the Poincaré sphere, shown in Fig. 1(a). Any pure state of polarization can be represented in terms of the coordinates on the sphere: the polar angle 2χ and the azimuth angle 2θ. It is given by

$$\hat{e}_{\theta,\chi} = e^{+i\theta}\cos\chi\hat{e}_R + e^{-i\theta}\sin\chi\hat{e}_L, \tag{7}$$

where $\hat{e}_R$ and $\hat{e}_L$ represent the states of circular polarization, right (RCP) and left (LCP), respectively [31]. Angle χ varies between 0 and $\pi/2$. The usefulness of this representation is that the two variables, χ and θ, specify the shape and orientation of the ellipse, respectively. The ratio of the amplitudes of the polarization components is related to the ellipticity of the state by

$$\epsilon = \frac{b}{a} = \tan(\pi/4-\chi), \tag{8}$$

where a and b are the semimajor and semiminor axes of the ellipse, respectively. The orientation of the ellipse, defined by the angle that the semimajor axis forms with the x axis, is θ. Figure 1(b) shows a grid pattern of states of polarization as a function of χ and θ. A particular case of interest is the state of linear polarization (LP) ($\chi = \pi/4$) oriented by an angle θ.

3. Experimental Method

We prepared Poincaré beams using a simple method, shown schematically in Fig. 2(a). Light from a single-spatial-mode helium–neon laser was sent to a polarization interferometer. The input polarization was set to be linear oriented at $\pi/4$ with the horizontal. A first polarizing beam splitter split the light by polarization. Amplitude binary forked gratings placed in each of the arms, equidistant from the second polarizing beam splitter, encoded the spatial mode of the two components of the Poincaré beam. The fringe spacing of the two gratings was the same. This way, the first-order modes from each grating overlapped. These outputs constituted a class of Poincaré beams

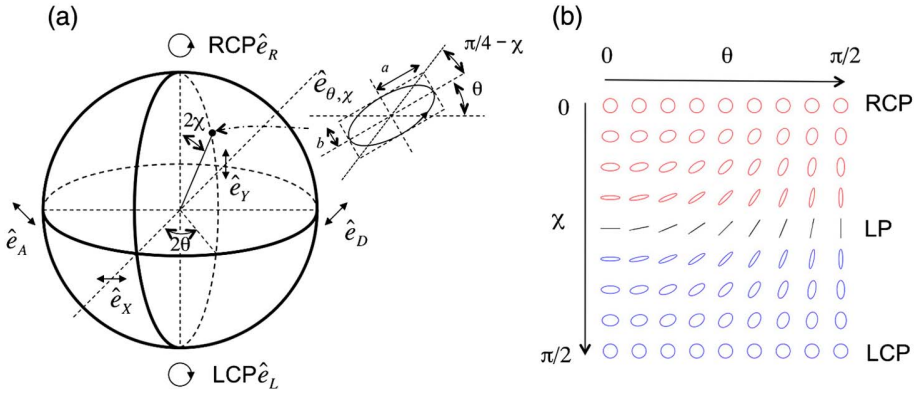

Fig. 1. (Color online) (a) Poincaré sphere showing how the states of polarization are represented on the surface of the sphere. (b) Matrix of polarization states obtained by varying the amplitude (vertical) and phase (horizontal) between component circular-state modes [see Eq. (7)]. Red and blue colors represent right-handed and left-handed polarization states, respectively, whereas black represents linear polarization.

that were encoded with the linear polarization basis. To encode the modes with the circular polarization basis, we added a quarter-wave plate after the interferometer, with its fast axis at $\pi/4$ with the horizontal.

We imaged the resulting modes with a digital camera. As seen in Fig. 2, the intensity of the mode is deceptively uniform, hiding rich polarization patterns within. We diagnosed the polarization state of the mode by passing the light through an arrangement of wave plates and a fixed Glan–Thompson polarizer before the camera. A single half-wave plate rotated by an angle $\beta/2$ served, in conjunction with the polarizer, as a linear polarizer analyzer oriented by β.

We also had the option of adding a second half-wave plate and a quarter-wave plate to block any desired state of polarization and thus have an intensity minimum appear in the imaged beam profile where the light had the selected polarization state. The

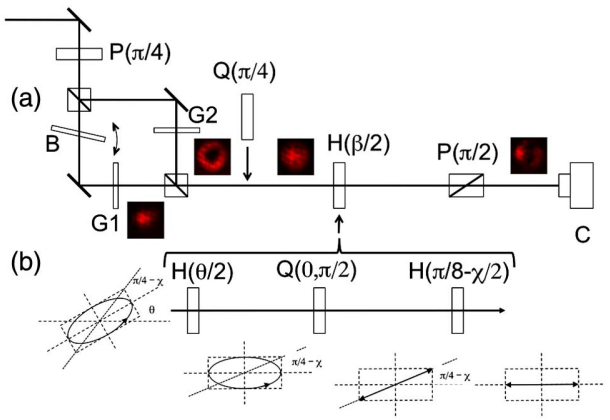

Fig. 2. (Color online) Schematic of the apparatus. (a) General setup to produce and diagnose vector modes and (b) arrangement to exclude specific polarization states. Optical components include forked gratings (G1 and G2), glass blank (B), polarizers (P), half-wave plate (H), quarter-wave plate (Q), and digital camera (C).

arrangement is shown in Fig. 2(b). The advantage of this method is that, by rotating the first half-wave plate, we varied the orientation of the semimajor axis of the selected elliptically polarized state and, by rotating the second half-wave plate, we varied the ellipticity of the state via χ.

4. Poincaré Beams

We produced Poincaré beams by combining Laguerre–Gauss modes with orthogonal polarization states. We used two polarization bases: circular (R, L) and linear (X, Y), but other elliptical polarization bases can be used [31]. A Poincaré mode produced this way has the form

$$V_{p_1,\ell_1,p_2,\ell_2} = \frac{1}{\sqrt{2}}(LG^{\ell_1}_{p_1}e^{i\alpha}\hat{e}_R + LG^{\ell_2}_{p_2}e^{-i\alpha}\hat{e}_L) \quad (9)$$

with the circular basis or

$$W_{p_1,\ell_1,p_2,\ell_2} = \frac{1}{\sqrt{2}}(LG^{\ell_1}_{p_1}e^{i\alpha}\hat{e}_X + LG^{\ell_2}_{p_2}e^{-i\alpha}\hat{e}_Y) \quad (10)$$

with the linear basis.

We divide the results into three sets. The first two consist of modes that have spatial modes with $p = 0$ in the circular and linear bases, and in the third case we explore the modes for $p \neq 0$. The first two are divided into two important subcases: when $\ell_1 \neq -\ell_2$ and $\ell_1 = -\ell_2$.

A. Circular Basis

1. *Case* $\ell_1 \neq -\ell_2$

The expression for the Poincaré mode in the circular basis is

$$V_{0,\ell_1,0,\ell_2} = \frac{G}{\sqrt{2}}(A_{0,\ell_1}r^{|\ell_1|}e^{i(\ell_1\phi+\alpha)}\hat{e}_R + A_{0,\ell_2}r^{|\ell_2|}e^{i(\ell_2\phi-\alpha)}\hat{e}_L). \quad (11)$$

This equation can be rewritten as

$$V_{0,\ell_1,0,\ell_2} = NGe^{i(\ell_1+\ell_2)\phi/2}(e^{i\theta}\cos\chi\hat{e}_R + e^{-i\theta}\sin\chi\hat{e}_L), \tag{12}$$

where

$$\chi = \tan^{-1}\frac{A_{0,\ell_2}r^{|\ell_2|}}{A_{0,\ell_1}r^{|\ell_1|}}, \tag{13}$$

$$\theta = (\ell_1 - \ell_2)\phi/2 + \alpha, \tag{14}$$

and N is a normalization factor. Referring to the general equation of the state of polarization, Eq. (7), the polarization state for this mode has an ellipticity [Eq. (8)] determined by χ in Eq. (13), which depends only on r. If $|\ell_1| < |\ell_2|$, then when $r \to 0$, the state of polarization is right circularly polarized (i.e., $\chi \to 0$). For values of r increasing from 0, the ellipticity decreases, with the polarization state remaining right handed. At the radius

$$r_v = \left(\frac{A_{0,\ell_2}}{A_{0,\ell_1}}\right)^{1/(|\ell_1|-|\ell_2|)}, \tag{15}$$

$\chi = \pi/4$, and the amplitude of the two spatial modes is the same. Therefore, the state of polarization is linear. For $r > r_v$ the polarization is left handed, with ellipticity decreasing and reaching -1 asymptotically when $r \to \infty$ ($\chi \to \pi/2$). In the figures the handedness is denoted by color (online only): red for right handed and blue for left handed. Because the orientation of the semimajor axis of the ellipse is given by θ in Eq. (14), it depends only on ϕ. Figure 3 shows the polarization maps for two cases: (a) $\ell_1 - \ell_2 = -1$ and (b) $\ell_1 - \ell_2 = +1$, where the semimajor axis of polarization rotates clockwise and counterclockwise by half a turn, respectively. When $\ell_1 - \ell_2 = 2$ (not shown here; see [31]), the polarization pattern has a radial look: the semimajor axis lies along radial lines.

Note also that the patterns correspond to a one-to-one mapping of points on the Poincaré sphere to points on the plane. When $|\ell_1 - \ell_2| = n > 1$, the Poincaré sphere is mapped onto n sectors, so a given state of polarization is mapped onto n points on the plane in regular angular intervals. Going from $r = 0$ to $r =$

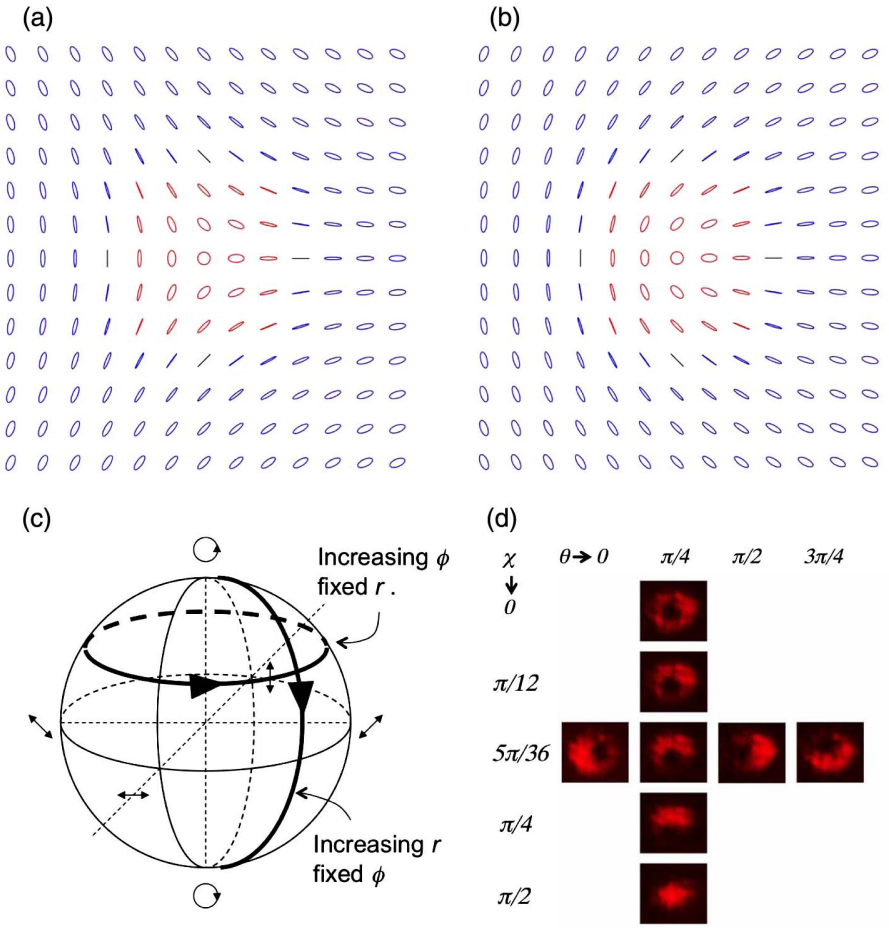

Fig. 3. (Color online) Polarization-state maps of the Poincaré mode obtained by combining spatial modes with (a) $\ell_1 - \ell_2 = -1$ and (b) $\ell_1 - \ell_2 = +1$. In both cases, the spatial modes have $p_1 = p_2 = 0$, and the polarization of the component modes is circular. (c) Poincaré sphere paths showing the sequence of states obtained by either increasing r with fixed ϕ or increasing ϕ with fixed r. (d) Images of the Poincaré mode with $\ell_1 = 0$ and $\ell_2 = 1$ after passage through a polarization-state analyzer, with settings specified by χ and θ.

∞ at fixed ϕ is equivalent to going from one pole of the Poincaré sphere to the other through a meridian, which is determined by ϕ, as shown in Fig. 3(c). Following the state of polarization in Figs. 3(a) and 3(b) along a circle centered at $r = 0$ corresponds to following a circular trajectory of constant latitude, as shown in Fig. 3(c).

Passage of this mode through a polarization-state analyzer, which blocks a unique state of polarization, results in n minima. If we rotate the analyzer angle, the minima rotate at the rate $d\phi_m/d\beta = 2/(\ell_1 - \ell_2)$. To verify this case, we created a Poincaré mode with $\ell_1 = 0$ and $\ell_2 = 1$. Figure 3(d) shows data taken with the state analyzer of Fig. 2(b) where we set the analyzer to block a polarization state specified by χ and θ. To simplify the diagnosis, we set the interferometer phase so that $\alpha = 0$. This way the radial and angular coordinates of minima were given by $r_m = \tan \chi/\sqrt{2}$ and $\phi_m = -2\theta$. For the left–right sequence of images, we selected the elliptically polarized state with ellipticity $\epsilon = 0.47$ ($\chi = 5\pi/36$) for four values of θ. We can see in the images that there is a minimum at $\phi_m = 0$ when $\theta = 0$. The minimum rotates clockwise by $\pi/2$ when the selected angle is increased counterclockwise by $\pi/4$. This is consistent with the map of Fig. 3(a). The top-down sequence of images in Fig. 3(d) correspond to $\theta = \pi/4$ and a variable ellipticity controlled by χ. We can see that, at $\chi = 0$, the minimum is at the center, consistent with eliminating the state of right-circular polarization. We see the minimum moves from the center to the periphery of the mode as χ is increased, consistent with the map of Fig. 3(a) and following the meridian with $2\theta = \pi/2$. When $\chi = \pi/2$, there is no minimum, as the state of left-circular polarization is located at $r_m = \infty$.

This case produces Poincaré modes that have elliptical singularities, C-points, at their center. Figures 3(a) and 3(b) are the iconic "star" and "lemon" polarization singularities [20]. The C-points are singular in the orientation of the ellipse axes, since these are undefined for circular polarization. The orientation of the ellipses around the C-point rotate $n/2$ times per turn around it [29], clockwise and counterclockwise in Figs. 3(a) and 3(b), respectively. At the radius r_v, we observe another type of polarization singularity: L-lines. These are lines of linear polarization that separate regions of different elliptical handedness [21].

2. *Case* $\ell_1 = -\ell_2$

We can express the Poincaré mode for this case as

$$V_{0,\ell,0,-\ell} = \frac{A_{0,\ell} r^{|\ell|} G}{\sqrt{2}} (e^{i(\ell\phi+\alpha)} \hat{e}_R + e^{-i(\ell\phi+\alpha)} \hat{e}_L), \tag{16}$$

$$= A_{0,\ell} r^{|\ell|} G \hat{e}_{(\ell\phi+\alpha),\pi/4}, \tag{17}$$

where $\ell = \ell_1 = -\ell_2$. The amplitude of the mode, given by Eq. (17), is a single ring that peaks at r_ℓ [Eq. (6)]. The state of polarization is linear because at every point there is an equal mixture of right and left circularly polarized states. Thus, we can refer to this type of mode as a vector mode. The orientation of the linear polarization is independent of r and forms an angle $\ell\phi + \alpha$ with the X axis. Figure 4(a) shows the calculated pattern for $\ell = +3$. As ϕ is increased for $r \neq 0$, the state of polarization follows a path along the equator of the Poincaré sphere, as shown in Fig. 4(b). The polarization axis performs 2ℓ half turns around the center of the beam, or revolutions along the equator of the Poincaré sphere. Note that there is no polarization state drawn at the center of the map (beam) of Fig. 4(a). That point is a Poincaré–Hopf polarization vector singularity or V-point [29,32] because it has all the linear polarization orientations.

We diagnosed this mode by imaging it after passage through a linear polarizer analyzer forming an angle β with the horizontal (X axis). The transmitted intensity is proportional to $\cos^2(\ell\phi + \alpha - \beta)$. It has 2ℓ minima at angles

$$\phi_m = \frac{(2m-1)\pi}{2\ell} - \frac{\alpha}{\ell} + \frac{\beta}{\ell}, \tag{18}$$

where $m = 1, 2 \ldots 2\ell$. As we vary β, the minima rotate at the rate $d\phi_m/d\beta = 1/\ell$. This is shown in Fig. 4(c). The minima also rotate at the same rate in the opposite direction when the interferometer phase is increased.

For $\ell = 1$ the vector-mode patterns have been studied before: for $\alpha = 0$ the mode is the well studied radial vector mode, and for $\alpha = \pi/2$ it is the azimuthal vector mode. The modes transmitted by the polarizer are the first-order Hermite–Gauss spatial modes rotated by β [33].

B. Linear Basis

This subsection covers patterns that are quite distinct from the previous sections. These patterns do not have the same type of symmetry about the center of the beam as the previous modes.

1. *Case* $\ell_1 \neq -\ell_2$

The Poincaré mode for this case is

$$W_{0,\ell_1,0,\ell_2} = \frac{G e^{i(\ell_1+\ell_2)\phi/2}}{\sqrt{2}} (A_{0,\ell_1} r^{|\ell_1|} e^{i(\ell_1-\ell_2)\phi/2+\alpha} \hat{e}_X + A_{0,\ell_2} r^{|\ell_2|} e^{-i(\ell_1-\ell_2)\phi/2-\alpha} \hat{e}_Y). \tag{19}$$

To understand this equation better, we can rewrite it as

$$W_{0,\ell_1,0,\ell_2} = NG e^{i(\ell_1+\ell_2)\phi/2} (e^{i\theta'} \cos\chi' \hat{e}_X + e^{-i\theta'} \sin\chi' \hat{e}_Y), \tag{20}$$

where $\chi' = \chi$ and $\theta' = \theta$ are defined by Eqs. (13) and (14), respectively. However, χ' and θ' do not relate to the ellipticity and orientation of the semimajor axis of the ellipses because the polarization eigenstates

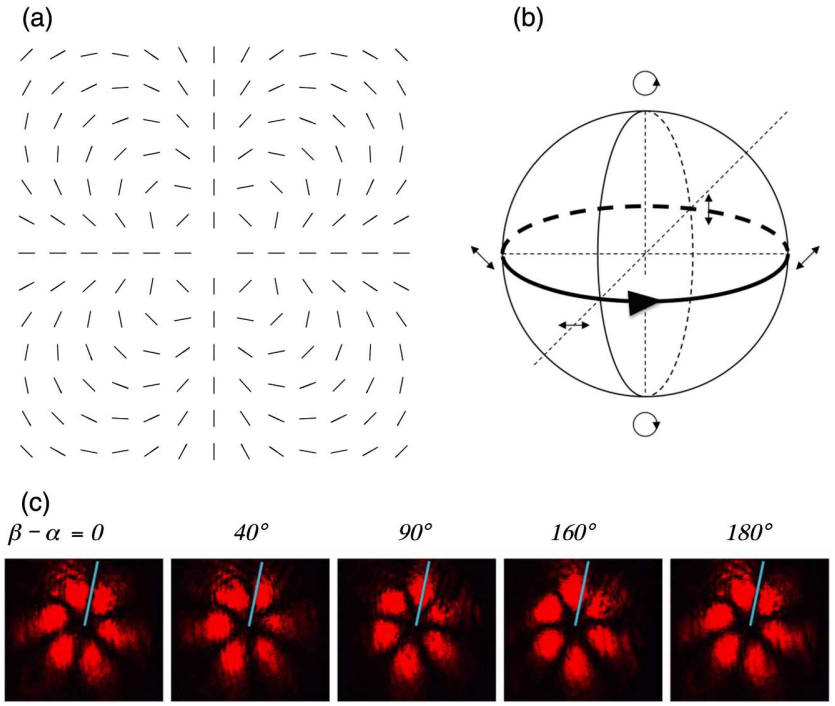

Fig. 4. (Color online) Vector mode obtained by combining $\ell_1 = +3$ and $\ell_2 = -3$ spatial modes in the circular polarization basis: (a) polarization-state map, (b) path that the state of polarization follows on the Poincaré sphere for a circular path about the center of the beam (i.e., increasing ϕ at fixed r), and (c) images of the vector mode obtained after passage through a polarizer in several orientations β.

are $\hat{e}_X$ and $\hat{e}_Y$ instead of $\hat{e}_R$ and $\hat{e}_L$. If $|\ell_1| < |\ell_2|$, then when $r \to 0$, $\chi' \to 0$, and so the state of polarization, defined by Eq. (20), is $\hat{e}_X$; and when $r \to \infty$, leading to $\chi' \to \pi/2$, the state of polarization becomes $\hat{e}_Y$. Figure 5 shows the polarization maps for two cases within the choice $|\ell_1| < |\ell_2|$: (a) $\ell_1 - \ell_2 = 1$ and (b) $\ell_1 - \ell_2 = 2$. For r increasing from 0, with $\phi = 0$, the map shows that the polarization axis rotates counterclockwise in both cases. We can identify the change in the state of linear polarization with a path on the Poincaré sphere: going from $\hat{e}_X$ to its antipode, $\hat{e}_Y$, by taking a path along the equator of the sphere. More generally, all radial trajectories starting from the center of the beam correspond to great semicircles on the Poincaré sphere that start with $\hat{e}_X$ at $r = 0$ and end with $\hat{e}_Y$ at $r = \infty$, as shown in Fig. 5(c). The sequence of states in the beam at $\phi = \theta'$ correspond to the states along the great semicircle shown in the figure. When $\phi = m\pi/2$ in Fig. 5(a) and $\phi = m\pi/4$ in Fig. 5(b) (with m an odd integer), the great semicircle passes through a pole of the sphere at $r = r_v$ on its way to $\hat{e}_Y$.

The sequence of states along a circular path about the center of the beam correspond to the states along the circular trajectory on the Poincaré sphere shown in Fig. 5(c). Short of a demonstration, we can understand this by recognizing that the form of Eq. (20) is identical to that of Eq. (12), with $2\chi'$ and $2\theta'$ being the polar and azimuth angles on the sphere, respectively, now defined by a polar axis ($\chi' = 0$) along $\hat{e}_X$ and a $\theta' = 0$ axis along $\hat{e}_D$. This also helps us visualize the polarization patterns that we would get if we selected other elliptically polarized eingenstates (antipodal on the sphere) as the polarization eigenstates to combine with spatial modes [31].

Figure 5(d) shows a few measurements verifying the pattern of Fig. 5(b). In the case shown, $\alpha \neq 0$. We obtained the image by nulling a linear polarization state. That is, the image detects states on the Poincaré sphere of Fig. 5(c) with $\theta' = 0, \pi/2$. We do so by varying χ', which depends on r. Thus, by varying the orientation of the nulled state, the minima move radially from image to image. Experimentally we varied θ from $\pi/4$ to $-\pi/4$ for $\chi = \pi/4$, which was equivalent to varying χ' from $\pi/4$ to 0 for $\theta' = 0$, followed by increasing χ' from 0 to $\pi/4$ for $\theta' = \pi/2$. Thus, the minima moved first inward at $\phi = \alpha$ and then outward at $\phi = \alpha + \pi/2$.

We note that, for the case of circular polarization bases, α added to the orientation of the ellipses [see Eqs. (12) and (17)]. Thus, the pattern rotated rigidly with α. However, in the case of the linear bases with $\chi' = \pi/4$, a phase α produced rotations of the pattern in a different way: the *positions* of the states rotated, but the states themselves retained their orientation. This can be appreciated by the form of Eq. (20). Thus, in the case of Fig. 5(d), the adjustment of the orientation of the nulled linear polarization state was independent of the value of α. A change in α still produced a rotation in the orientation of the minima but not on the orientation of the state being blocked. The specific images in the figure were allowed to saturate the digital camera to better appreciate the motion of the minima. Figure 2 shows the unsaturated images for

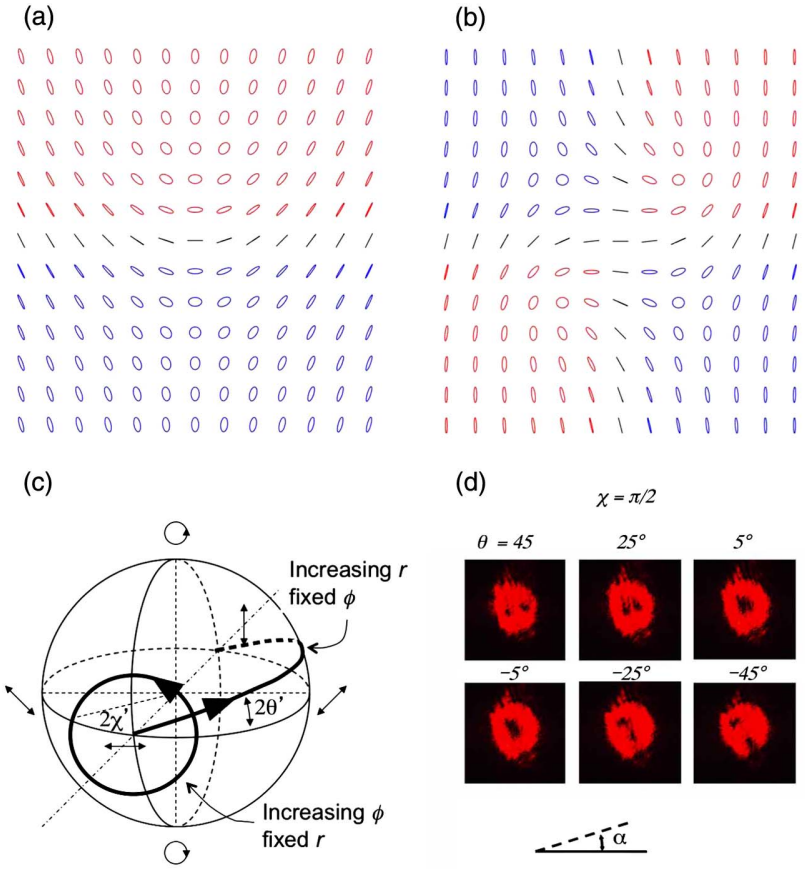

Fig. 5. (Color online) Polarization-state maps of the Poincaré mode obtained by combining spatial modes with (a) $\ell_1 - \ell_2 = 1$ and (b) $\ell_1 - \ell_2 = 2$. In both cases the spatial modes have $p_1 = p_2 = 0$ and $|\ell_1| < |\ell_2|$ with the polarization of the component modes linear. (c) Poincaré sphere paths for states with increasing r with fixed ϕ and increasing ϕ with fixed r. (d) Measurements of the Poincaré mode involving the superposition of spatial modes with $\ell_1 = 0$ and $\ell_2 = -2$ in the linear basis. Images show the mode that passed a linear polarization analyzer oriented an angle β. The phase between the two modes was 2α, with $\alpha \sim 22°$.

the modes corresponding to this case: the component modes, the Poincaré mode, and the mode after passage through an analyzer set to 130°.

This case shows interesting patterns of polarization singularities: C-point dipole and quadrupole in Figs. 5(a) and 5(b), respectively, with L-lines dividing elliptical regions of same handedness. Passage of these Poincaré modes through a state analyzer still contains interesting patterns of singularities: scalar singularities. For example, if the light in the state of Eq. (10) passes through a linear polarization analyzer oriented at an angle β, the state emerging from the polarizer is

$$W'_{0,\ell_1,0,\ell_2} = (LG^{\ell_1}_{p_1} e^{i\alpha} \cos\beta + LG^{\ell_2}_{p_2} e^{-i\alpha} \sin\beta)\hat{e}_\beta, \quad (21)$$

which is a superposition of Laguerre–Gauss modes with relative weights determined by β. The resulting spatial mode is well known [34,35]: a pattern of phase vortices of topological charge ℓ_1 at $r = 0$ surrounded by $|\ell_1 - \ell_2|$ vortices of topological charge $\ell_2/|\ell_2|$ located at $r = r_v$ and angularly equidistant.

2. *Case* $\ell_1 = -\ell_2$

If we combine spatial modes in orthogonal linearly polarized states, the vector mode is given by

$$W_{0,\ell,0,-\ell} = \frac{A_{0,\ell} r^{|\ell|} G}{\sqrt{2}} (e^{i(\ell\phi+\alpha)}\hat{e}_X + e^{-i(\ell\phi+\alpha)}\hat{e}_Y). \quad (22)$$

Converting the previous equation to the circular basis yields

$$W_{0,\ell,0,-\ell} = A_{0,\ell} r^{|\ell|} Gi[e^{-i\pi/4} \cos(\ell\phi + \alpha - \pi/4)\hat{e}_R + e^{i\pi/4} \sin(\ell\phi + \alpha - \pi/4)\hat{e}_L], \quad (23)$$

$$= A_{0,\ell} r^{|\ell|} G\hat{e}_{-\pi/4,\ell\phi+\alpha-\pi/4}. \quad (24)$$

The mode represented by Eq. (24) has the shape of a ring with a maximum amplitude at $r = r_\ell$. The polarization is independent of r but dependent on ϕ. Recalling Eqs. (7) and (8), the ellipticity of the beam depends on ϕ via

$$\chi = \ell\phi + \alpha - \pi/4. \quad (25)$$

Figure 6(a) shows the polarization map for $\ell = 2$. To simplify the analysis, we set $\alpha = 0$, so $\chi = 2\phi - \pi/4$. This way, at $\phi = 0$, the polarization is linear and oriented diagonal. (If we force χ to be positive, then $\chi = \pi/4$ and $\theta = \pi/4$.) At $\phi = \pi/8$ the polarization is right circular. At $\phi = \pi/4$, the polarization is linear again, but antidiagonal. Because χ increases with ϕ, as given by Eq. (25), the polarization state around the center of the beam follows a path on the Poincaré sphere along the meridians with $2\theta = \pm\pi/2$, as shown in Fig. 6(b), and completes ℓ revolutions on the sphere per turn around the beam. You can appreciate this in the four colored sectors (in online version) of Fig. 6(a).

This type of mode has been referred to as the hybrid vector mode for the case $\ell = 1$ [8,33], where at angles when χ is a multiple of $\pi/2$ the polarization is circular, at angles when χ is an odd multiple of $\pi/4$ the polarization is linear, and at other angles the polarization is elliptical, with semimajor axis oriented at either $+\pi/4$ (diagonal) or $-\pi/4$ (antidiagonal) with the horizontal.

Figure 6(c) shows the measurements of the beam transmitted through a linear polarization analyzer oriented an angle β. The first panel is the transmission through a polarizer set to $\beta = 0$. This setting does not produce any minima. When we set the linear polarization analyzer to $\beta = \pi/4$, all the antidiagonal states of polarization are blocked. Thus, we see four minima at the predicted angles (i.e., $\phi = m\pi/4$, m odd). By following the polarization-state map, we see that, at $\phi = \pi/2$, there is no minima again. We can understand this more easily by realizing that, at $\beta = 0$, $\pi/2$, we are completely blocking one of the component spatial modes and transmitting fully the other one. When we set β to $3\pi/4$, we can see from the map that the states cancelled are at $\phi = n\pi/2$ (n integer), as seen in the images. For completeness, we include images at other intermediate angles to show that the minima for those cases do not reach zero. It can be shown that the modes seen for $\beta = \pi/4$ and $\beta = 3\pi/4$ are the unrotated and rotated, respectively, second-order Hermite–Gauss mode with indices $(1, 1)$.

Notice that, as with a previous case, the polarization state located in the middle of the pattern is missing because it is a singular point. It is a point that has *all* ellipticities: the states along the great circle of Fig. 6(b). This can be interpreted as a Stokes singularity [36,37] because $S_1 = 0$, whereas S_2 and S_3 are undefined [38].

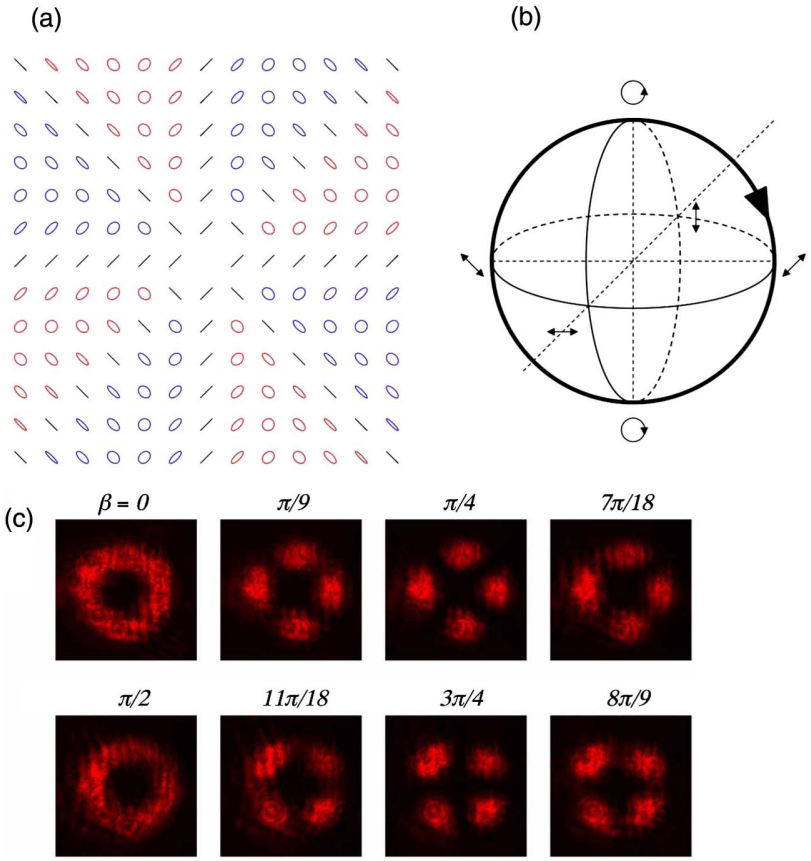

Fig. 6. (Color online) (a) Polarization-state map obtained by combining $\ell_1 = 2$ and $\ell_2 = -2$ spatial modes in the linear polarization basis, (b) path on the Poincaré sphere followed by the state of polarization of points of increasing transverse angle ϕ and fixed radius r, and (c) images of the vector mode obtained after passing it through a polarizer in several orientations β.

C. Multiringed Modes

We now discuss one further generalization of our Poincaré modes: allowing cases where the component Laguerre–Gauss modes have $p \neq 0$. Consider the case where we superimpose a mode with $p = 0$ and $\ell \neq 0$ with the mode with $p \neq 0$ and $\ell = 0$. This combination produces an interesting result that we analyze. At $r = 0$ the spatial mode is purely the one with $p \neq 0$. This is because the one with $\ell \neq 0$ has zero amplitude at that point. The mode with $p \neq 0$ has p radial nodes, with adjacent radial sectors out of phase by π.

As an example, let us consider the case where the spatial modes are LG_0^1 and LG_1^0 in right- and left-circular polarizations, respectively. The Poincaré mode for this case is

$$W_{0,1,1,0} = \frac{Ge^{i\phi/2}}{\sqrt{2}}[A_{0,1}re^{i(\phi/2+\alpha)}\hat{e}_R + A_{1,0}(-2r^2+1)e^{-i(\phi/2+\alpha)}\hat{e}_L], \quad (26)$$

or

$$W_{0,1,1,0} = NGe^{i\phi/2}(\cos\chi'' e^{i\theta''}\hat{e}_R + \sin\chi'' e^{-i\theta''}\hat{e}_L), \quad (27)$$

with

$$\tan\chi'' = \frac{A_{1,0}(-2r^2+1)}{A_{0,1}r}, \quad (28)$$

$$\theta'' = \phi/2 + \alpha. \quad (29)$$

It produces the polarization map shown in Fig. 7(a). The polarization state starts as left circular at $r = 0$ [$\chi'' = \pi/2$ in Eq. (27)]. As r increases, the polarization state at fixed ϕ changes following a meridian on the Poincaré sphere [Fig. 7(b)], starting from the south pole and reaching the north pole (i.e., right-circular polarization) when $r = r_\ell = 1/\sqrt{2}$. LG_1^0 mode has a node at the latter radius. Within this radius, the beam has nonzero intensity everywhere and contains *all* the states on the Poincaré sphere. As r increases past r_ℓ, the polarization state continues with the meridian at the opposite side of the sphere and reaching the south pole at $r \to \infty$. Thus, the polarization pattern of this mode is a mapping of the Poincaré sphere onto two radial sectors on the beam. By varying the values of the ℓ of the component spatial modes, we can add angular sectors and multiply further the mapping of the Poincaré sphere onto points in the transverse plane.

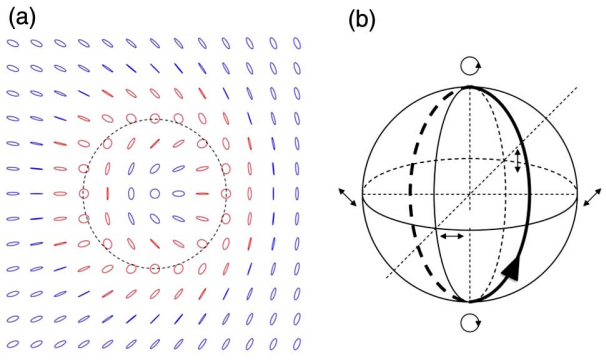

Fig. 7. (Color online) (a) Polarization map of modes with $p_1 = 0$, $\ell_1 = 1$ and $p_2 = 1, \ell_2 = 0$ in the circular basis. The circle drawn has radius r_ℓ. (b) Path taken on the Poincaré sphere when following a radial trajectory.

5. Discussion and Conclusions

As has been shown in this article, both theoretically and experimentally, a relatively simple experimental setup can be used to produce a rich variety of Poincaré modes by varying the indices of the component spatial modes and the polarization bases. We explained the polarization patterns of the Poincaré modes via trajectories on the Poincaré sphere.

Our analysis did not consider propagation effects but considered the effects of a phase between the component spatial modes. Upon propagation, the relative phase of the spatial modes of different order changes due to the Gouy phase. As a consequence, we expect Poincaré mode patterns in these cases to rotate accordingly [35], with noted exceptions.

We were able to produce many types of polarization singularities: V-points, where the orientation of linearly polarized states is undefined; C-points, where the orientation of polarization ellipses is undefined; L-lines, where the handedness of the ellipses is undefined; and a type of Stokes singularity where two Stokes parameters are undefined. The only singularity that we were not able to reproduce with our method was the monstar (see for example [29]). This is because we limited ourselves to Laguerre–Gauss eigenmodes for the component spatial modes, but mixing superpositions with opposite polarization states should provide the proper setting. Thus, our method can be used as the basis to study all types of polarization singularities. To our knowledge, this is a first demonstration of a method to produce any polarization singularities on demand.

One could consider using this method to encode information in the polarization pattern of Poincaré modes. It would be interesting to determine how stable these patterns are under propagation in inhomogeneous media. We can envision preparing particular Poincaré modes, launch them into an inhomogeneous or birefringent medium, and study the evolution of the pattern and the singularities contained within.

Further work on the investigation of polarization singularities should involve noncollinear propagation. This setting will allow investigation of new three-dimensional polarization singularities predicted recently: Móbius strips of linear polarization [39].

This work was funded by National Science Foundation grant PHY-0903972 and U. S. Air Force

contract FA8750-11-2-0034. We thank David L. Andrews, Patrick Crotty, and Francisco De Zela for valuable advice and discussions.

References

1. Y. Mushiake, K. Matsumura, and N. Nakajima, "Generation of radially polarized optical beam mode by laser oscillation," Proc. IEEE **60**, 1107–1109 (1972).
2. M. Stalder and M. Schadt, "Linearly polarized light with axial symmetry generated by liquid-crystal polarization converters," Opt. Lett. **21**, 1948–1950 (1996).
3. S. C. Tidwell, D. H. Ford, and W. D. Kimura, "Generating radially polarized beams interferometrically," Appl. Opt. **29**, 2234–2239 (1990).
4. R. Oron, S. Blit, N. Davidson, A. A. Friesem, Z. Bomzon, and E. Hasman, "The formation of laser beams with pure azimuthal and radial polarization," Appl. Phys. Lett. **77**, 3322–3324 (2000).
5. K. S. Youngsworth and T. G. Brown, "Focusing of high numerical aperture cylindrical vector beams," Opt. Express **7**, 77–87 (2000).
6. S. Quabis, R. Dorn, M. Eberler, O. Glöckl, and G. Leuchs, "Focusing light to a tighter spot," Opt. Commun. **179**, 1–7 (2000).
7. A. M. Beckley, T. G. Brown, and M. A. Alonso, "Full Poincaré beams," Opt. Express **18**, 10777–10785 (2010).
8. Q. Zhan, "Cylindrical vector beams: from mathematical concepts to applications," Adv. Opt. Photon. **1**, 1–57 (2009).
9. C. Maurer, A. Jesacher, S. Fürhapter, S. Bernet, and M. Ritsch-Marte, "Tailoring of arbitrary optical vector beams," New J. Phys. **9**, 78 (2007).
10. S. C. McEldowney, D. M. Shemo, and R. A. Chipman, "Vortex retarders produced from photo-aligned liquid crystals polymers," Opt. Express **16**, 7295–7308 (2008).
11. Z. Bomzon, G. Biener, V. Kleiner, and E. Hasman, "Radially and azimuthally polarized beams generated by space variant dielectric subwavelength gratings," Opt. Lett. **27**, 285–287 (2002).
12. T. A. Fadeyeva, V. G. Shvedov, Y. V. Izdebskaya, A. V. Volyar, E. Brasselet, D. N. Neshev, A. S. Desyatnikov, W. Krolikowski, and Y. S. Kivshar, "Spatially engineered polarization states and optical vortices in uniaxial crystal," Opt. Express **18**, 10848–10863 (2010).
13. G. Volpe and D. Petrov, "Generation of cylindrical vector beams with few-mode fibers excited by Laguerre–Gaussian beams," Opt. Commun. **237**, 89–95 (2004).
14. G. Milione, H. I. Sztul, R. R. Alfano, and D. A. Nolan, "Stokes polarimetry of a hybrid vector beam from a spun elliptical core optical fiber," Proc. SPIE **7613**, 761305 (2009).
15. S. Ramachandran, P. Kristensen, and M. F. Yan, "Generation and propagation of radially polarized beams in optical fibers," Opt. Lett. **34**, 2525–2527 (2009).
16. J. R. Fontana and R. H. Pantell, "A high-energy laser accelerator for using the inverse Cherenkov effect," J. Appl. Phys. **54**, 4285–4288 (1983).
17. S. Quabis, R. Dorn, and G. Leuchs, "Generation of a radially polarized doughnut mode of high quality," Appl. Phys. B **81**, 597–600 (2005).
18. J. F. Nye, "Line singularities in wave fields," Proc. R. Soc. A **387**, 105–132 (1983).
19. J. F. Nye, "Lines of circular polarization in electromagnetic wave fields," Proc. R. Soc. A **389**, 279–290 (1983).
20. J. F. Nye, *Natural Focusing and Fine Structure of Light* (IOP, 1999).
21. M. V. Berry and M. R. Dennis, "Polarization singularities in isotropic random vector waves," Proc. R. Soc. A **457**, 141–155 (2001).
22. M. S. Soskin, V. Denisenko, and I. Freund, "Optical polarization singularities and elliptic stationary points," Opt. Lett. **28**, 1475–1477 (2003).
23. F. Flossmann, U. T. Schwarz, M. Maier, and M. R. Dennis, "Polarization singularities from unfolding an optical vortex through a birefringent crystal," Phys. Rev. Lett. **95**, 253901 (2005).
24. R. I. Egorov, M. S. Soskin, D. A. Kessler, and I. Freund, "Experimental measurements of topological singularity screening in random paraxial scalar and vector optical fields," Phys. Rev. Lett. **100**, 103901 (2008).
25. F. Flossmann, K. O'Holleran, M. R. Dennis, and M. J. Padgett, "Polarization singularities in 2D and 3D speckle fields," Phys. Rev. Lett. **100**, 203902 (2008).
26. M. Burresi, R. J. P. Engelen, A. Opheij, D. van Oosten, D. Mori, T. Baba, and L. Kuipers, "Observation of polarization singularities at the nanoscale," Phys. Rev. Lett. **102**, 033902 (2009).
27. I. O. Buinyi, V. G. Denisenko, and M. S. Soskin, "Topological structure in polarization resolved conoscopic patterns for nematic liquid crystal cells," Opt. Commun. **282**, 143–155 (2009).
28. Y. V. Jayasurya, V. V. G. Krishna Inavalli, and N. K. Viswanathan, "Polarization singularities in the two-mode optical fiber output," Appl. Opt. **50**, E131–E137 (2011).
29. I. Freund, "Polarization singularity indices in Gaussian laser beams," Opt. Commun. **201**, 251–270 (2002).
30. M. W. Beijersbergen, L. Allen, H. E. L. O. van der Veen, and J. P. Woerdman, "Astigmatic laser mode converters and transfer of orbital angular momentum," Opt. Commun. **96**, 123–132 (1993).
31. E. J. Galvez and S. Khadka, "Poincaré modes of light," Proc. SPIE **8274**, 83740Y (2012).
32. I. Freund, "Polarization flowers," Opt. Commun. **199**, 47–63 (2001).
33. E. J. Galvez, "Vector beams in free space," in *The Angular Momentum of Light*, D. L. Andrews and M. Babiker, eds. (Cambridge, to be published).
34. E. J. Galvez, N. Smiley, and N. Fernandes, "Composite optical vortices formed by collinear Laguerre–Gauss beams," Proc. SPIE **6131**, 613105 (2006).
35. S. M. Baumann, D. M. Kalb, L. H. MacMillan, and E. J. Galvez, "Propagation dynamics of optical vortices due to Gouy phase," Opt. Express **17**, 9818–9827 (2009).
36. I. Freund, "Poincaré vortices," Opt. Lett. **26**, 1996–1998 (2001).
37. I. Freund, A. I. Mokhum, M. S. Soskin, O. V. Angelsky, and I. I. Mokhum, "Stokes singularity relations," Opt. Lett. **27**, 545–547 (2002).
38. I. Freund, M. S. Soskin, and A. I. Mokhum, "Elliptic critical points in paraxial optical fields," Opt. Commun. **208**, 223–253 (2002).
39. I. Freund, "Möbius strips and twisted ribbons in intersecting Gauss–Laguerre beams," Opt. Commun. **284**, 3816–3845 (2011).